

# Electronic topological transitions and vibrational properties of A-15 type $X_3Y$ ( $X = V, Cr$ and $Mo$ ; $Y = Os, Ir$ and $Pt$ ) compounds: A first-principles study

P. Rambabu<sup>a,b</sup>, Giuseppe Zollo<sup>c</sup>, V. Kanchana<sup>a,\*</sup>

<sup>a</sup> Department of Physics, Indian Institute of Technology Hyderabad, Kandi, 502285, Sangareddy, Telangana, India

<sup>b</sup> Department of Pure and Applied Physics, Guru Ghasidas Vishwavidyalaya, Koni, Bilaspur, 495009, Chhattisgarh, India

<sup>c</sup> Dipartimento di Scienze di Base e Applicate per L'Ingegneria, Università di Roma "La Sapienza", Via A. Scarpa 14-16, 00161, Rome, Italy

## ARTICLE INFO

### Keywords:

Fermi surface  
Electronic topological transition  
Electron-phonon coupling  
Superconductivity

## ABSTRACT

Ab-initio studies of A-15 type  $X_3Y$  ( $X = V, Cr$  and  $Mo$ ;  $Y = Os, Ir$  and  $Pt$ ) compounds are presented at ambient and high pressures. All the studied compounds satisfy the mechanical stability criteria and are also dynamically stable as evidenced from the positive phonon dispersion curves. Camels back type band structure features are observed at Fermi level in some of the investigated compounds. Electronic topological transitions (ETTs) are the main highlights in all the compounds under pressure at different compressed volumes. The electron-phonon coupling constants  $\lambda$  are calculated on the basis of the Eliashberg theory for the  $Mo_3Y$  ( $Y = Os, Ir$  and  $Pt$ ) series that, according to the experiments, have the largest transition temperature among the studied compounds.  $Mo_3Os$  superconductivity is fully understood on the basis of the Eliashberg theory of the phonon-mediated electron pairing and the experimental  $T_c$  is recovered using the well known Mc Millan formula. On the contrary, for the other two compounds of the same series  $Mo_3Y$  ( $Ir$  and  $Pt$ ) the calculated mass enhancement parameters show an unexpected behavior and for  $Mo_3Ir$ , the experimental transition temperature values cannot be easily recovered through the Mc Millan formula.

## 1. Introduction

A-15 compounds such as  $X_3Y$  ( $X = V, Nb, Cr, Ti, Mo, Zr, Ta, W$  to  $Hf$  and  $Y = Al, Ga, Ge, In, Sn, Os, Ir, Pt$  etc.) are quite popular as they could be explored for their high superconducting transition temperature ( $T_c$ ). The structure of A-15  $X_3Y$  compounds can be viewed as  $X$  atoms forming orthogonal chain like structure along the axes and are found to possess low site symmetry, which may lead to the observed high  $T_c$  values. The 'd' electrons of the  $X$ -atom contribute to a greater extent around the Fermi level ( $E_F$ ). In some compounds,  $T_c$  increases as the size and mass of the  $Y$  element decreases for a given  $X$  element. Recent studies on the X-ray photo-emission spectra of A-15 type  $Nb_3(Os, Ir, Pt)$  compounds indicated that 4d states of  $Nb$  and 5d states of  $Y$  ( $Os, Ir, Pt$ ) appear to be more and more separated as the atomic number of the  $Y$  element increases [1].

The study of A-15 superconducting properties mainly demands the understanding of the electronic and lattice dynamical properties of such compounds. For instance there are reports evidencing flat bands close to

Fermi level ( $E_F$ ) giving rise to sharp peaks in the density of states  $N(E_F)$  leading to a high value of  $T_c$  [2,3], thus supporting the idea that flat bands may be a common feature in these compounds. Hein et al. [5] reported that superconductivity in  $Cr_3Ir, Cr_3Rh, Nb_3Os, V_{1-x}Ni_x, V_3Pd$  and  $Ta_{85}Pt_{15}$  compounds is not necessarily due to electronic density of states  $N(E_F)$  alone, but also may arise from phonon frequencies, which principally determines the strength of electron-phonon coupling  $\lambda$ , and hence  $T_c$ . Recently, it has been reported that A-15  $V_3S$  is a BCS-type superconductor with strong electron-phonon coupling [6] and that  $T_c$  degradation in stoichiometric disordered A-15  $Nb_3Sn$  compound is due to the suppression of electron-phonon coupling [7].

Concerning the role of the electronic structure, and of the shape of the Fermi surface (FS) at or near the Fermi level [8], a notable point, first stated by Lifshitz [9], is that chemical or thermal pressure may cause the FS change and then the metal's behavior. These phenomena are known as Electronic Topological Transitions (ETTs) and in the recent literature there are many reports on that. Ghosh et al. [10] showed that Ba site being doped with small amount of Sn in  $BaFe_2As_2$  leads to ETTs. Jarlborg

\* Corresponding author.

E-mail address: [kanchana@phy.iith.ac.in](mailto:kanchana@phy.iith.ac.in) (V. Kanchana).

<https://doi.org/10.1016/j.jpcs.2021.109953>

Received 15 August 2020; Received in revised form 7 January 2021; Accepted 9 January 2021

Available online 1 February 2021

0022-3697/© 2021 Elsevier Ltd. All rights reserved.

et al. [11] found that an ordered H<sub>3</sub>S lattice shows multiple Lifshitz transitions as a function of pressure which leads to high  $T_c$  superconducting behavior. Zhang et al. [12] provided a direct proof for the Lifshitz transition induced by temperature in ZrTe<sub>5</sub>, thus explaining, in a quite natural way, the origin of resistivity anomaly in this compound. It has been shown, also, that under pressure around 1.2 GPa, semiconductor black-phosphorus undergoes an ETT [13] and subsequently undergoes a semi-metallic transition above this pressure characterized by novel electronic states and properties. In yet another study, the authors found that a similar topological transition can be observed in Dirac Semimetal Na<sub>3</sub>Bi [14], as a function of the binding energy. FS topological transition is observed in bulk Rashba spin-split BiTeCl [15]. The compound Sb<sub>2</sub>S<sub>3</sub> [16] is found to undergo two phase transitions at high pressures around 5 GPa and 15 GPa and the authors reported an ETT in this compound near 5 GPa. The authors have predicted ETTs under pressure in Nb-based [17] A-15 superconducting compounds Nb<sub>3</sub>X (X = Al, Ga, In, Ge, and Sn), and all these studies significantly project the importance of ETTs and need to be explored carefully.

Then, in the present work, the A-15 compounds X<sub>3</sub>Y (X = V, Cr and Mo; Y = Os, Ir and Pt) are analyzed, where X and Y belongs to the transition metal series and Y atoms are heavier than X ones. More specifically, two important objectives are addressed: the first one is to focus on electronic topological transitions (ETTs) of A-15 compounds under pressure through Fermi surface topology and mechanical properties and the second one being the analysis of superconducting properties of these compounds at ambient pressure in terms of electron-phonon coupling constant  $\lambda$ , as we find a large variation in  $T_c$  among the analyzed compounds. A possible reason for the drastic variation in  $\lambda$ , and hence  $T_c$  is speculated by the analysis of phonon spectra and the vibrational modes.

## 2. Computational details

Density Functional theory using the Full-Potential Linearized Augmented Plane Wave (FP-LAPW) method together with PBE-GGA [18] (Perdew-Burke-Ernzerhof) has been performed using WIEN2K [19] to compute the ground state properties and the elastic tensor. The radius of the atoms ( $R_{MT}$ ) are 1.80 *a. u.* for V and Cr; 2.0 *a. u.* for Mo; and 2.30 *a. u.* for Os, Ir and Pt atoms respectively for the entire calculations and for the convergence, we have set the criteria as  $R_{MT}^*K_{max} = 7$ , where  $K_{max}$  is the plane wave cut-off. The Fourier expansion of the potential and charge density were carried out till  $G_{max} = 12 \text{ a. u.}^{-1}$ . A dense mesh of  $44 \times 44 \times 44$  grid of k points in the Monkhorst-Pack [20] scheme gave 2300 k-points in the irreducible part of the Brillouin Zone (IBZ) and the same was used for the entire calculations. Brillouin zone integration was carried out using the tetrahedron method [21]. In order to ensure proper energy convergence we have set it as  $10^{-5}$  Ry for the self consistent calculations. Birch-Murnaghan [22] equation of state was used to obtain the ground state properties for the investigated compounds. Calculations including spin-orbit coupling (SOC) were also performed which led to significant changes at the Fermi level in band structure and hence in Fermi surface topology and we proceeded with further calculations including SOC. The phonopy [23] software is used with VASP [24] to calculate the phonon dispersion and the Force Constants (FC's) in the context of Density Functional Perturbation Theory (DFPT). Phonon calculations have been performed in a  $2 \times 2 \times 2$  super cell with a  $4 \times 4 \times 4$  q-point mesh. The calculated FC's are further used in phonopy to calculate phonon DOS with a sampling mesh of  $16 \times 16 \times 16$ . The electron-phonon coupling constants, the mass enhancement parameters and  $T_c$  values are calculated from the Eliashberg theory of phonon assisted superconductivity [25] using the Quantum Espresso suite [26]. The calculations have been performed in the context of PBE-GGA approximation, using ultrasoft pseudopotentials, with a k-point mesh of  $16 \times 16 \times 16$  for convergence of the DFPT problem and a q-point mesh of  $2 \times 2 \times 2$ . Because these calculations are quite computationally demanding, we have limited them only to the Mo<sub>3</sub>Y (Y = Os, Ir, Pt) series at ambient as this series is the one with the highest  $T_c$  values with respect

to the ones considered in the present study.

## 3. Results and discussions

The A-15 compounds X<sub>3</sub>Y (X = V, Cr, Mo and YOs, Ir, Pt) exist in cubic structure with space group  $Pm\bar{3}n$  (223) where X and Y atoms occupy respectively the (1/4, 0, 1/2) and (0, 0, 0) positions in the corresponding conventional unit cell that is shown, together with the corresponding Brillouin zone, in Fig. 1. The calculated results are given in Table 1 and are in good accord with other available data as given in the same table. The computed bulk modulus follows a decreasing trend in all of X<sub>3</sub>Y compounds, when Y changes from Os to Pt. In the same way, bulk modulus values are increasing from X = V to Cr and to Mo. Among all the compounds, Mo<sub>3</sub>Os and V<sub>3</sub>Pt have the highest and the lowest bulk modulus values. All these compounds are quite stable as it is evaluated by looking at the crystal elastic constants reported in Table 2 together with earlier reports. These calculated values are satisfying the Born stability criteria [27]. The calculated Young's modulus is highest, and nearly the same, for all the Cr based compounds making these compounds stiffer than others. The computed elastic anisotropy factor reveals the extent of anisotropy in the present compounds. Cauchy's pressure ( $C_{11}-C_{44}$ ) being positive is an indication that the studied compounds are ductile, and the Pugh's ratio further confirms the same. If this ratio is less than 0.57, the compound tends to be ductile. The Poisson's ratio taking the values in between -1 and 0.5, with -1 as the lower limit, can be used to predict the behavior of the compound against shear, and in the present case, we infer that all the compounds of the present study might be stiffer.

### 3.1. Electronic properties at ambient pressure

The electronic structure properties of X<sub>3</sub>Y (X = V, Cr, Mo and Y = Os, Ir, Pt) compounds are analyzed from the band structures plotted along different high symmetry directions as shown in Fig. (2), (4) and (5) together with the density of states (DOS) plots given in Fig. (S1,S2,S3) of Supplementary sheet. For the sake of comparison and better understanding, we try to explain the bands of V<sub>3</sub>Y (Y = Os, Ir, Pt), then we present the bands of Cr<sub>3</sub>Y (Y = Os, Ir, Pt) and Mo<sub>3</sub>Y (Y = Os, Ir, Pt) as they both are almost similar belonging to the same column in the periodic table.

The calculated total DOS and projected DOS as a function of energy E (eV) are shown in Fig. (S1,S2,S3). The higher non-zero value of the total density of states (TDOS) at  $E_F$  is a clean evidence for the metallic nature present in these compounds. From the reported values of TDOS given in Table 1, it can be seen that the value decreases from Os to Ir and increases again in the case of Pt. This can be well understood from the DOS plots as we observe the  $E_F$  to lie on the shoulder in V<sub>3</sub>Os, which shifts to a pseudo gap in the case of Ir and again gets positioned on the peak leading to the maximum density of states in the case of V<sub>3</sub>Pt. In addition, it also very vivid that both the valence band (VB) and conduction bands (CB) are dominated by the contributions from V-atoms. In both V and Y-atoms, the 3d-states of V and 5d-states of Y are found to play the dominant role with a very small contribution from s and p-states of V and Y-atoms. The peaks present in the energy range from 0 to 2 eV mainly arises from the strong hybridization between the V-d states and d-states of Y-atoms.

The band structure of V<sub>3</sub>Y along the high symmetry directions are shown in Fig. 2(a,b,c), where we could visualize the VB and CB to overlap leading to zero band gap. One common feature which is present in these A-15 compounds is the presence of flat bands near the  $E_F$  which is very clearly seen in V<sub>3</sub>Pt, leading to the peaks in DOS plots just close to  $E_F$ . Yet another noticeable feature present in these compounds would be the clustering of bands around X and M points, which is also observed in V<sub>3</sub>Y series.

Fermi surface studies of a metallic system is inevitable as all the

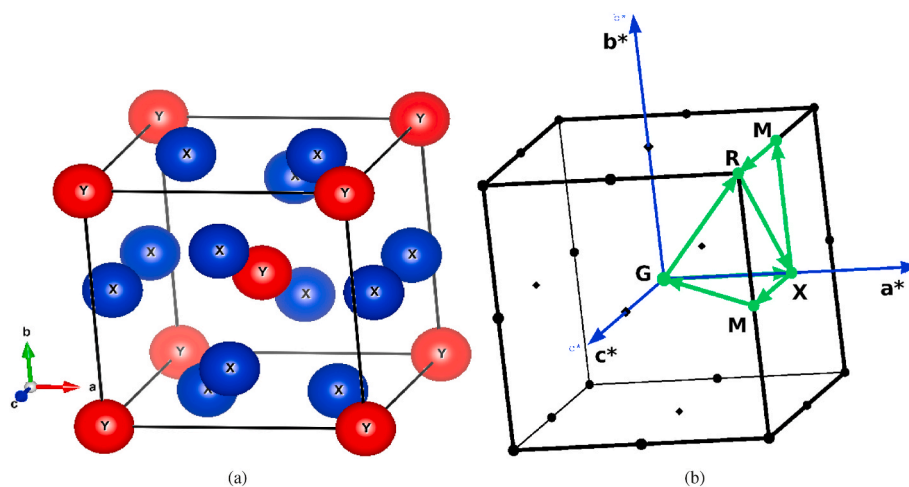


**Fig. 1.** (a) The conventional unitcell of A-15 compound  $X_3Y$  ( $X = V, Cr, Mo$  and  $Y=Os, Ir, Pt$ ). (b) The Brillouin Zone of  $XY$  compounds with different high symmetry points.

**Table 1**

Ground state properties of  $X_3Y$  ( $X = V, Cr, Mo$ ;  $Y = Os, Ir, Pt$ ) at ambient pressure combined with experimental and other theory reports and are given in the brackets.  $a_{th}$  is theoretical lattice parameter in  $\text{\AA}$ ,  $B$  is bulk modulus in  $GPa$ ,  $N$  ( $E_F$ ) is total density of states at  $E_F$  in the units of  $states/eV/cell$ . and  $\gamma_{th}$  is the theoretical Sommerfield coefficient in  $mJ/molK^2$ .

Parameters	$a_{th}$	$B$	$N(E_F)$	$\gamma_{th}$
$V_3Os$	4.778 (4.8480 [3])	243	7.85	18.51
$V_3Ir$	4.778 (4.7850,4.780 [3])	242	4.45	10.50
$V_3Pt$	4.805 (4.808)	223	10.15	23.93
$Cr_3Os$	4.637 (4.6840)	289	14.42	34.00
$Cr_3Ir$	4.639 (4.6850)	281	11.16	26.32
$Cr_3Pt$	4.666 (4.7120)	257	15.28	36.02
$Mo_3Os$	4.985 (4.9693,4.9492 [4])	290 (301.7 [4])	8.85	20.87
$Mo_3Ir$	4.984 (4.9580,4.9430 [4])	284 (297.5 [4])	8.58	20.25
$Mo_3Pt$	5.003 (4.9870,4.9552 [4])	264 (287.1 [4])	8.54	20.14

physical properties of the system is dependent on the Fermi surface topology. Here also the three-dimensional Fermi surfaces of  $V_3Y$  are shown in Fig. 3(a,b,c). The number of bands which cross the  $E_F$  are found to be four, three and three for  $V_3Os$ ,  $V_3Ir$  and  $V_3Pt$  respectively as shown in Fig. 2(a,b,c) and the corresponding Fermi surfaces are shown in Fig. 3 (a,b,c). It is clear that the Fermi surfaces contain both electron and hole sheets. The Fermi surface corresponding to band number one in all  $V_3Os$  compound possesses hole-like sheets around M-point. The Fermi surface topology of second band in  $V_3Os$  compound is more complex with hole sheet around M-point and electron-like sheets at X and R-points. The third band possesses tiny electron-sheets around R and X with a complex electron sheet around zone center. The fourth band possesses an electron sheet at  $\Gamma$ -point. These Fermi surfaces are well comparable with the earlier report [28]. The main change noticed in the band structure of

**Table 2**

Single crystalline elastic constants of  $X_3Y$  ( $X = V, Cr, Mo$ ;  $Y = Os, Ir, Pt$ ) at ambient pressure in  $GPa$ ,  $E$  is Young's modulus in  $GPa$ ,  $\sigma$  is Poisson's ratio,  $A$  is Anisotropy factor, CP= Cauchy's pressure ( $C_{11}-C_{44}$ ) in  $GPa$ , PR= Pugh's ratio and  $\theta_D$  is Debye temperature in  $Kelvin$ .

Parameters	$C_{11}$	$C_{12}$	$C_{44}$	$E$	$A$	CP	PR	$\sigma$	$\theta_D$
$V_3Os$	451	141	91	293	0.585	49.78	0.46	0.299	363.11
$V_3Ir$	468	127	112	336	0.651	14.98	0.55	0.267	390.86
$V_3Pt$	423	121	95	293	0.629	26.03	0.52	0.279	363.34
$Cr_3Os$	484	191	124	345	0.846	67.57	0.45	0.301	386.04
$Cr_3Ir$	502	170	116	346	0.700	54.56	0.48	0.294	386.31
$Cr_3Pt$	507	135	108	343	0.579	26.82	0.51	0.278	386.16
$Mo_3Os$	516	175	101	326	0.595	75.16	0.43	0.312	330.17
$Mo_3Ir$	508	169	89	311	0.535	76.38	0.42	0.316	321.61
$Mo_3Pt$	495	148	90	308	0.521	57.62	0.45	0.306	320.46

$V_3Ir$  is that the X and R points are completely free and the same is noticed in the respective Fermi surfaces. The first band of  $V_3Os$  leads to a small electron pocket at M together with a sheet along X-M. Here also, we visualize a solid electron sheet at  $\Gamma$  similar to  $V_3Os$  due to second band in Fig. 2(b). The third band in  $V_3Ir$  leads to electron sheets along  $\Gamma$ -X. In the case of  $V_3Pt$  from Fig. 2(c), the first band leads to tiny hole pockets along M-R. The second band leads to the two split complicated Fermi surfaces. The third band possesses a pocket at X, which is found to expand along  $\Gamma$ -X-M direction.

Now we would like to move ahead with  $Cr_3Y$  and  $Mo_3Y$  compounds as shown in Fig. 4(a,b,c) and Fig. 5(a,b,c) respectively. Similar to  $V_3Y$ , here also one could observe the total DOS value to decrease from Os to Ir and to increase for Pt case. We also observe the Fermi level  $E_F$  to be situated at the pseudo gap for the Ir case, while it is on the shoulders in the other two cases. The total DOS values are found to be highest for  $Cr_3Y$  compared to  $V_3Y$  and  $Mo_3Y$  series. In the case of  $Mo_3Y$  series, we do not observe the sudden drop in total DOS value as seen in  $V_3Y$  and  $Cr_3Y$  series. The reason could be that  $E_F$  either lies at or close to peak and does not get positioned in pseudo gap. In both Cr and Mo-series also, the X atom contribution is found to be more pronounced as in the case of V-series. But one could see that the Y atom is found to contribute more in  $Mo_3Y$  series as compared to  $V_3Y$  and  $Cr_3Y$  series. One could also see the clustering of the bands around R, X and M points in both Cr and Mo-series, a feature present in A-15 compounds. One more interesting point to note is that the bands are comparatively flatter for  $Cr_3Y$  series which leads to multiple peaks in the DOS close to  $E_F$  and could lead to higher DOS in this case as observed from the values reported in Table 1.

Now we focus on the Fermi surfaces of  $Cr_3Y$  as shown in Fig. 6(a,b,c), where again we see four bands to cross  $E_F$  for  $Cr_3Os$ . The first band is a combination of hole and electron surfaces leading to electron pockets along  $\Gamma$ -R together with the hole sheets centered at R along with tiny

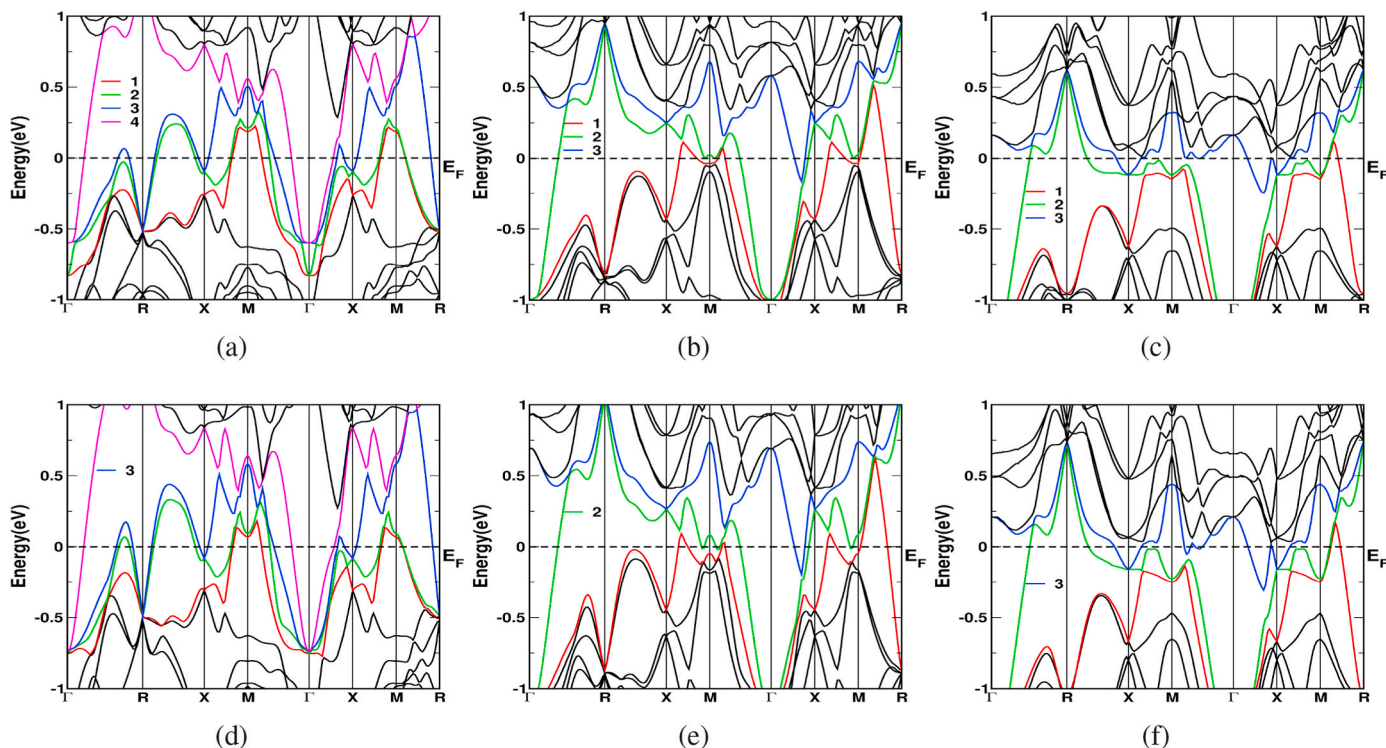


Fig. 2. Band structures of  $V_3Os$ ,  $V_3Ir$  and  $V_3Pt$  at ambient in (a), (b) and (c) and at  $V/V_0 = 0.90$  in (d), (e) and (f) respectively.

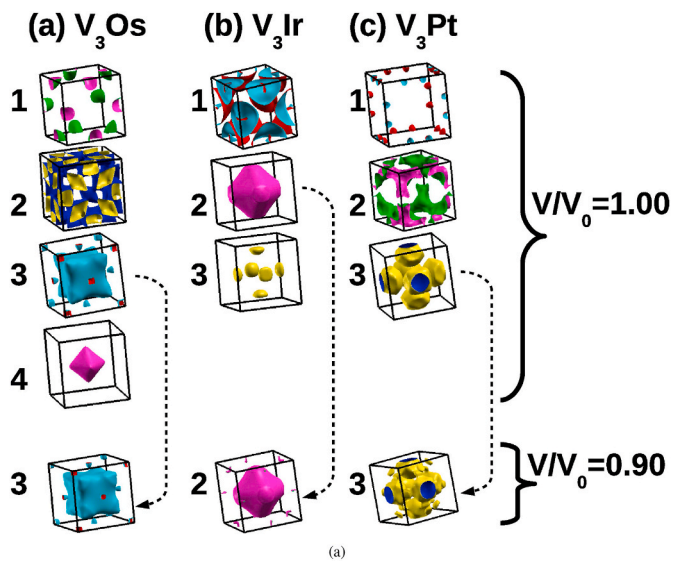


Fig. 3. Fermi surface topology of  $V_3Os$ ,  $V_3Ir$  and  $V_3Pt$  in (a), (b) and (c) at ambient and  $V/V_0 = 0.90$  respectively. The dashed arrow line indicates the Electronic Topological Transition upon compression.

pockets noticed between M and R points. The second and third bands cross  $E_F$  at several points leading to complicated Fermi surfaces as shown in Fig. 6(a). The fourth band has a tiny electron sheet at X and another electron surface along  $\Gamma$ -X placed close to X. In the case of  $Cr_3Ir$  from Fig. 4(b), we could find six bands to cross  $E_F$ . The first two bands lead to small hole-like sheets at R. The third and fourth bands cross  $E_F$  at several high symmetry points leading to complex Fermi surface as shown in Fig. 6(b) and the fourth band forms an electron sheet at X. The next bands five and six are also found to possess electron pocket at X and can be seen from Fig. 4(b). In the case of  $Cr_3Pt$  from Fig. 4(c), again six bands cross  $E_F$  and first two bands lead to very tiny electron pockets at R as

shown in Fig. 6(c). The third band has a very small hole contribution at M together with electron sheet along M-R and hole sheet close to R. The fourth and fifth bands lead to complicated surfaces as shown in Fig. 6(c). The last sixth band leads to electron sheet at X-point.

We compare the Fermi surfaces of  $Mo_3Y$  with  $Cr_3Y$  from Fig. 6(a,b,c, d,e,f) and we see that the Fermi surfaces of  $Mo_3Os$  is almost similar to  $Cr_3Os$  as seen Fig. 6(a,d) except for a very tiny changes. When we move ahead with Ir, we see only five bands to cross  $E_F$  in case of  $Mo_3Ir$  (Fig. 6 (e)) whereas six bands are found to cross  $E_F$  in  $Cr_3Ir$  (Fig. 6(b)). The only main difference in  $Mo_3Ir$  is that the sixth band does not cross  $E_F$  at X leading to the absence of the sixth Fermi surface which is an electron sheet at X in  $Cr_3Ir$ . When we move ahead with Pt, we find six Fermi surfaces for both  $Mo_3Pt$  and  $Cr_3Pt$  as shown in Fig. 6(f,c) except that there is a slight difference in third and fourth Fermi surfaces. There are small tiny pockets along M-R in third Fermi surface of  $Cr_3Pt$  which is absent in  $Mo_3Pt$  and additional pockets found in fourth Fermi surface of  $Mo_3Pt$  is absent in  $Cr_3Pt$ .

From the above discussion, it can be stated that  $Cr_3Pt$  and  $V_3Ir$  have the highest and lowest  $N(E_F)$  values. It is also observed that the variation of  $N(E_F)$  is very small for  $Mo_3Y$  compounds and this variation is more pronounced in  $V_3Y$  and  $Cr_3Y$  compounds which attracts further analysis in these compounds as there is a drastic variation in superconducting transition temperature in these compounds, which will be discussed in the next section.

### 3.2. Vibrational and superconducting properties at ambient pressure

All the A-15 compounds here considered are superconductors [29, 30], and the transition metals components as well, except for Cr and Pt. It is a general belief that superconductivity in  $A_3B$  A-15 compounds is phonon driven. However the Matthias rule [31] shows that the superconducting transition temperature is a two peaked function of the number of electrons per unit cell and this behavior cannot be explained on the simple electron-phonon interaction. Concerning the  $A_3B$  compounds (A transition metal and B non transition metal) a strong electron coupling in the context of the Hubbard Emery model is necessary to

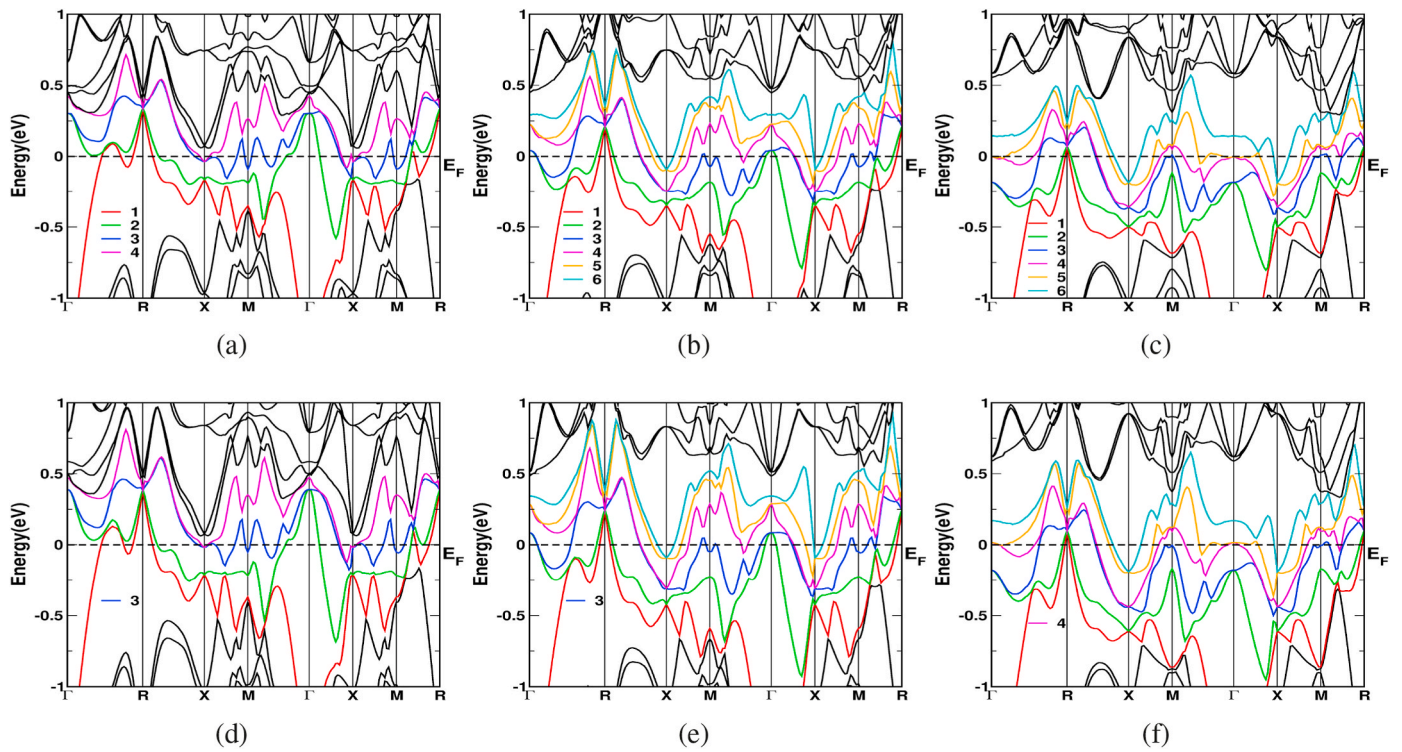


Fig. 4. Band structures of  $\text{Cr}_3\text{Os}$ ,  $\text{Cr}_3\text{Ir}$  and  $\text{Cr}_3\text{Pt}$  at ambient in (a), (b) and (c) and at  $V/V_0 = 0.90$  in (d), (e) and (f) respectively.

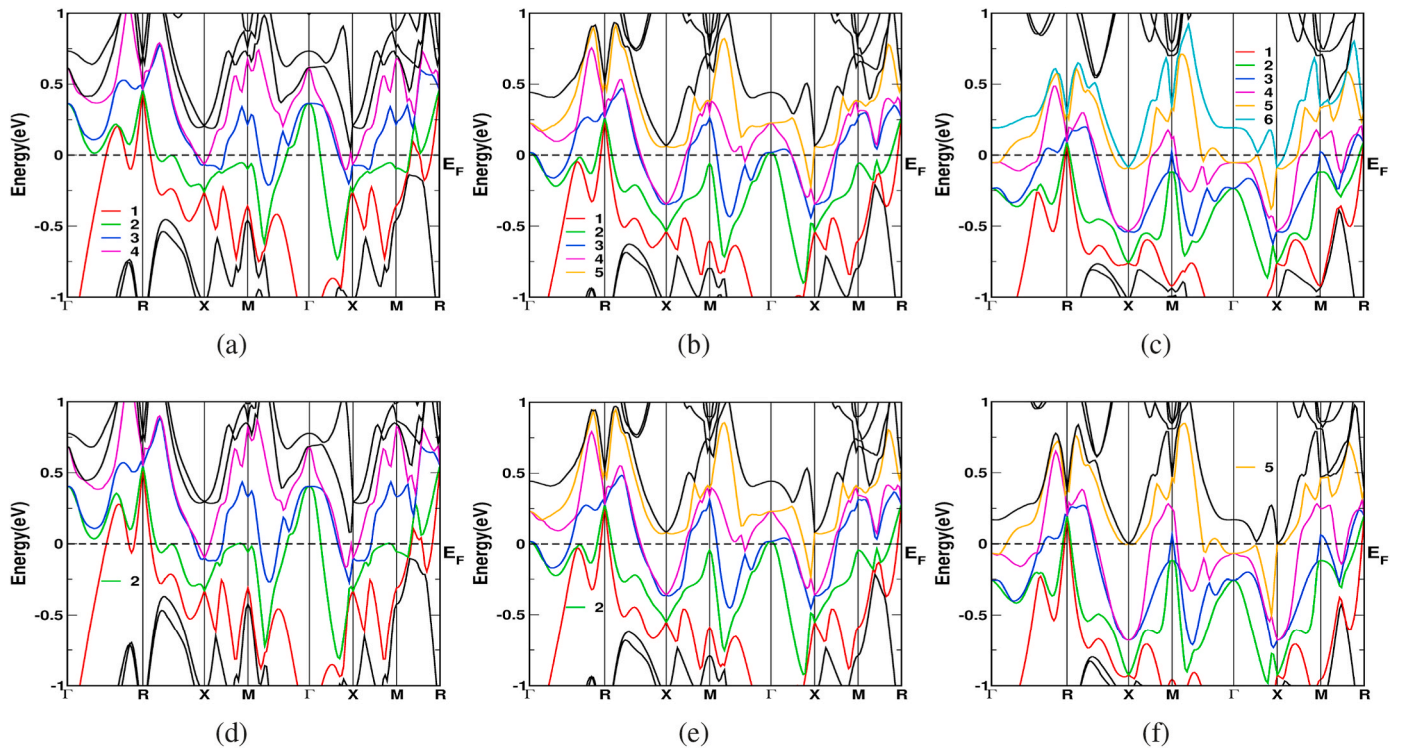


Fig. 5. Band structures of  $\text{Mo}_3\text{Os}$ ,  $\text{Mo}_3\text{Ir}$  and  $\text{Mo}_3\text{Pt}$  at ambient in (a), (b) and (c) and at  $V/V_0 = 0.92$ ,  $0.98$  and  $0.90$  in (d), (e) and (f) respectively.

justify the Matthias rule [32]. However, it is unclear whether this finding holds also for  $A_3B$  with A and B both transition metals. Hence, as a first approach for the considered transition metal compounds, we want to test the electron-phonon nature of the superconducting properties in the case of the Mo series, that is the one with the highest transition temperature values. The phonon dispersion spectra for Mo-series are

shown in Figs. 7(a) and 8(a) and 9(a) (see the supplementary information for the phonon bands of the other compounds in Fig S4, S5 and S6): as a general trend, the zone centered phonon modes of all the compounds can be represented as

$$\Gamma = 3T_{1u} + 2T_{2u} + T_{1g} + T_{2g} + A_{2g} + E_g \quad (1)$$

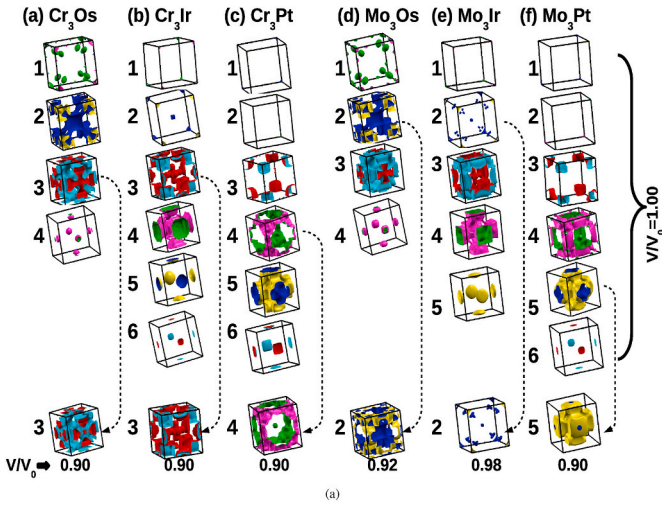


Fig. 6. Fermi surface topology of  $\text{Cr}_3\text{Os}$ ,  $\text{Cr}_3\text{Ir}$ ,  $\text{Cr}_3\text{Pt}$ ,  $\text{Mo}_3\text{Os}$ ,  $\text{Mo}_3\text{Ir}$  and  $\text{Mo}_3\text{Pt}$  in (a), (b), (c), (d), (e) and (f) at ambient and  $V/V_0=0.90$ ,  $0.90$ ,  $0.90$ ,  $0.92$ ,  $0.98$  and  $0.90$  respectively. The dashed arrow line indicates the Electronic Topological Transition upon compression.

where A, E and T are singly, doubly and triply degenerate phonon modes. The complete list of vibrational modes of  $\text{X}_3\text{Y}$  ( $\text{X} = \text{V}, \text{Cr}, \text{Mo}$ ;  $\text{Y} = \text{Os}, \text{Ir}, \text{Pt}$ ) compounds in  $\text{cm}^{-1}$  at ambient pressure is given in Table 3. Positive values of phonon frequencies indicate that all the compound are dynamically stable with the employed calculation parameters. In the  $\text{Mo}_3\text{Ir}$  case, however, the ultrasoft pseudopotentials have revealed unsuitable to guarantee the dynamical stability of the compound, whatever the  $k$ -points mesh, cutoff and threshold parameters employed. Then in this case, we have employed Troulleir-Martins (TM) (not ultrasoft) and Hartwigsen, S. Goedecker, and J. Hutter (HGH) [33] pseudopotentials. A consistency check has been done by re-calculating the transition temperature and the mass enhancement parameter (see below) using both TM and HGH pseudopotentials also for  $\text{Mo}_3\text{Pt}$ , obtaining the same result got with ultrasoft pseudopotentials.

Phonon mediated superconductivity depends on matrix elements  $g_{ij,\nu}(\mathbf{q}, \mathbf{k} + \mathbf{q})$  describing the interaction between two electrons in the  $i$ -th

band, with energy  $\epsilon_{ik}$ , and in the  $j$ -th band with energy  $\epsilon_{j\mathbf{k}+\mathbf{q}}$  mediated by a phonon with energy  $\omega_\nu(\mathbf{q})$  and momentum  $\mathbf{q}$ . The coupling constants  $g_{ij,\nu}(\mathbf{q}, \mathbf{k} + \mathbf{q})$  enter into the phonon self-energy line width

$$\gamma_{\mathbf{q}\nu} = 2\pi\omega_{\mathbf{q}\nu} \sum_{ij} \int_{\text{BZ}} d^3k |g_{ij,\nu}(\mathbf{q}, \mathbf{k} + \mathbf{q})|^2 \delta(\epsilon_{ik} - \epsilon_F) \delta(\epsilon_{j\mathbf{k}+\mathbf{q}} - \epsilon_F) \quad (2)$$

that, summing over the phonon bands and  $\mathbf{q}$  points casts into the Eliashberg spectral function  $\alpha^2F(\omega)$ :

$$\alpha^2F(\omega) = \frac{1}{2\pi N(\epsilon_F)} \sum_{\mathbf{q}} \sum_{\nu} \delta(\omega - \omega_{\mathbf{q}\nu}) \frac{\gamma_{\mathbf{q}\nu}}{\hbar\omega_{\mathbf{q}\nu}} \equiv \sum_{\mathbf{q}} [\alpha^2F(\omega)]_{\mathbf{q}} \quad (3)$$

where  $\epsilon_F$  is the Fermi energy and  $N(\epsilon)$  is the electron density of states. Then the so called mass-enhancement parameter  $\lambda$  is calculated [25]:

$$\lambda = 2 \int \frac{\alpha^2F(\omega)}{\omega} d\omega = 2 \sum_{\mathbf{q}} \int \frac{[\alpha^2F(\omega)]_{\mathbf{q}}}{\omega} d\omega \quad (4)$$

Lastly, the mass enhancement parameter can be employed to calculate the critical temperature through the Allen-Dynes modification of the Mc Millan formula [34,35].

$$T_C = \frac{\omega_{\log}}{1.20} \exp\left(\frac{1.04(1 + \lambda)}{\lambda - \mu^*(1 + 0.62\lambda)}\right) \quad (5)$$

where

$$\omega_{\log} = \exp\left(\int \log(\omega) \frac{2}{\lambda} \frac{\alpha^2F(\omega)}{\omega} d\omega\right) \quad (6)$$

and the parameter  $\mu^*$  is the Coulomb potential obtained through the Bennemann-Garland formula [36,37].

$$\mu^* = \alpha \frac{N(E_F)}{1 + N(E_F)} \quad (7)$$

with  $\alpha$  chosen to make  $\mu^*$  consistent with the experimental value.

In Fig. 7(b), we show the Eliashberg spectral function for  $\text{Mo}_3\text{Os}$  together with the  $\mathbf{q}$ -decomposed and weighted  $[\alpha^2F(\omega)]_{\mathbf{q}}$  functions. According to Eq. (4), the contribution to the mass enhancement parameter is obtained from  $\frac{[\alpha^2F(\omega)]_{\mathbf{q}}}{\omega}$ . On this basis, the phonon modes contributing most to the mass electron pairing (nearly 65% of the mass enhancement

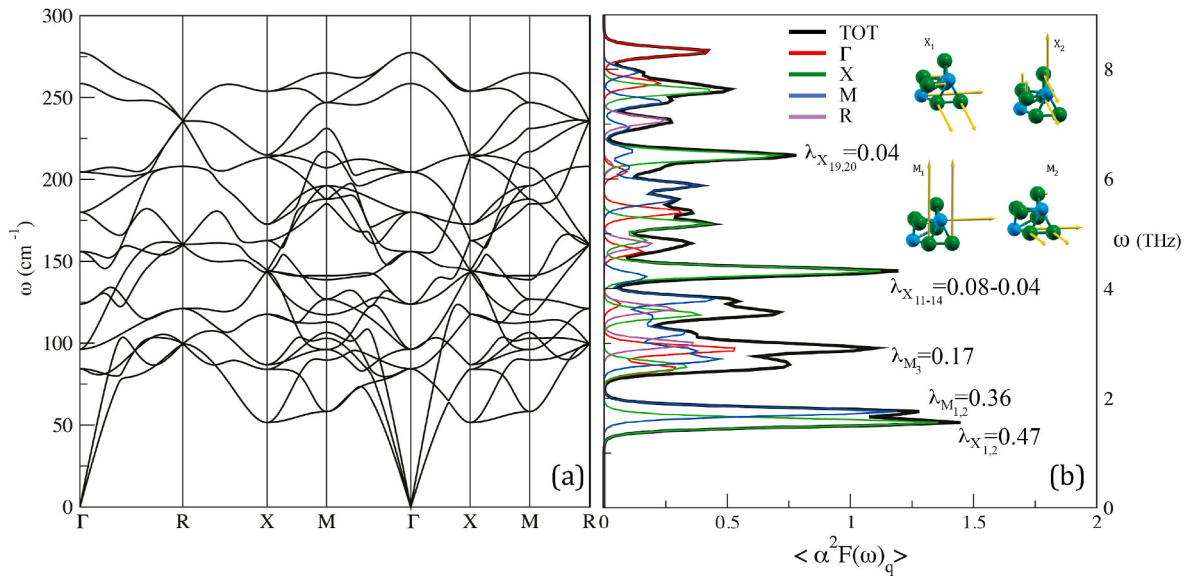
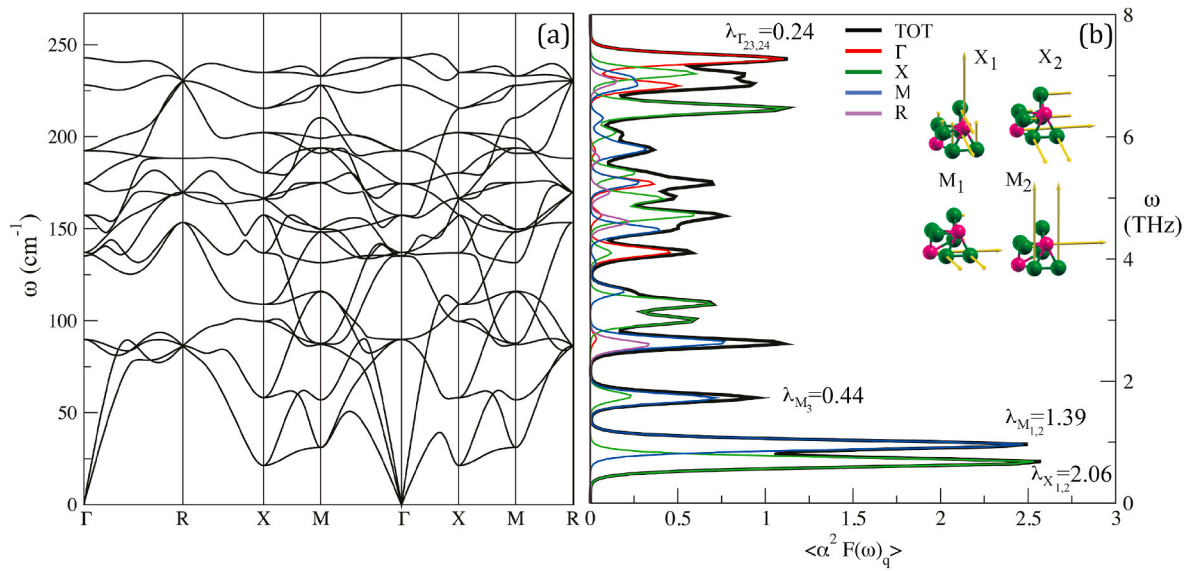


Fig. 7. Phonon dispersion (a) and total and  $\mathbf{q}$ -point resolved spectral function (b) for  $\text{Mo}_3\text{Os}$ . The most important vibrational eigen-vectors contributing to the phonon mediated coupling are drawn in the inset of (b). The peaks of the  $\mathbf{q}$ -point resolved spectral function are labeled with the main mode and  $\mathbf{q}$ -point resolved mass enhancement parameters  $\lambda_{\mathbf{q},\nu}$ .



**Fig. 8.** Phonon dispersion (a) and total and q-point resolved spectral function (b) for  $\text{Mo}_3\text{Pt}$ . The most important vibrational eigen-vectors contributing to the phonon mediated coupling are drawn in the inset of (b). The peaks of the q-point resolved spectral function are labeled with the main mode and q-point resolved mass enhancement parameters  $\lambda_{q,v}$ .

**Table 3**  
The vibrational modes of  $\text{X}_3\text{Y}$  ( $\text{X} = \text{V}, \text{Cr}, \text{Mo}$ ;  $\text{Y} = \text{Os}, \text{Ir}, \text{Pt}$ ) in  $\text{cm}^{-1}$  at ambient pressure.

Modes	$\text{V}_3\text{Os}$	$\text{V}_3\text{Ir}$	$\text{V}_3\text{Pt}$	$\text{Cr}_3\text{Os}$	$\text{Cr}_3\text{Ir}$	$\text{Cr}_3\text{Pt}$	$\text{Mo}_3\text{Os}$	$\text{Mo}_3\text{Ir}$	$\text{Mo}_3\text{Pt}$
$T_{1u}$	0.0	0.0	0.0	0.0	0.1	0.1	0.0	0.0	0.0
$T_{1u}$	182.3	165.6	152.7	167.8	159.2	165.1	126.0	123.4	134.7
$T_{1u}$	220.0	208.1	188.2	206.9	195.1	200.8	157.2	151.5	157.1
$T_{2u}$	141.5	133.4	86.8	111.1	95.9	83.6	88.4	87.2	89.2
$T_{2u}$	284.6	283.8	250.8	266.8	244.4	235.8	206.5	191.6	191.3
$T_{1g}$	234.2	235.2	156.8	148.3	177.3	208.3	101.4	107.2	137.0
$T_{2g}$	257.6	282.8	217.2	237.3	257.6	246.1	182.7	182.1	174.2
$A_{2g}$	349.9	336.9	261.7	216.6	171.1	160.0	259.6	$\approx 257.6$	222.0
$E_g$	330.9	337.1	292.7	197.5	235.4	213.8	276.6	280.6	239.8

parameter) are degenerate  $T_{1u}$  modes at the X-point ( $X_1, X_2$ ) and M-point ( $M_1, M_2$ ) reported in Table 4 together with the relevant quantities of the electron phonon coupling. Less important contributions come from degenerate modes at  $\omega = 2.89 \text{ THz}$  and  $\omega = 2.54 \text{ THz}$  at the  $\Gamma$  point (see the Supplementary Information Table. S1 for the complete list of q-point and mode resolved coupling parameters). As evidenced in inset of Fig. 7 (b), the main phonon mediated electron coupling just involves Mo atoms at the X-point while at the M point it involves both the species. The total mass enhancement parameter, with the density of states at the Fermi energy and logarithmic average, reported in Table 4 give a transition temperature value  $T_c = 12.8 \text{ K}$ , nicely close to the experimental value of  $T_c^{\text{exp}} = 12.7, 11.76 \text{ K}$  [30,32], by employing  $\mu^* = 0.15$ . The nice agreement of the prediction with the experimental value evidences the strong

**Table 4**  
Eliashberg main superconducting properties and parameters for  $\text{Mo}_3\text{Os}$ ,  $\text{Mo}_3\text{Ir}$  and  $\text{Mo}_3\text{Pt}$  compounds. The  $\sigma$  parameter is the gaussian broadening for the double delta sampling in Eq. 2

	$N(E_F)$ ( $eV^{-1}$ (u.c.) $^{-1}$ )	$\omega_{\log}$ (K)	$\lambda$	$\sigma$ (Ry)	modes	$\omega$ (THz)	$\lambda_{ep}$
$\text{Mo}_3\text{Os}$	7.75	130.9	1.51	0.03	$X_1, X_2$ $M_1,$ $M_2$	1.55 1.75	0.47 0.36
$\text{Mo}_3\text{Pt}$	7.95	56.17	2.68	0.03	$X_1, X_2$ $M_1,$ $M_2$	0.67 0.96	2.06 1.39
$\text{Mo}_3\text{Ir}$	5.96	242.7	0.54	0.045	$\Gamma_{10-12}$ $\Gamma_{13-15}$	4.9 5.51	0.1 0.12

coupling that, together with the large logarithmic average value, fully justifies the transition temperature value, in spite of the relatively low value of the density of states at the Fermi energy. Then we can state that the strong coupling involving the modes at X and M q-points is the origin of the superconducting behavior of this compound. In the case of  $\text{Mo}_3\text{Pt}$ , we got a quite large mass enhancement  $\lambda = 2.68$ . The total and the q-resolved spectral functions are reported in Fig. 8(b) while the most important modes, again the lowest  $T_{1u}$  ( $X_1, X_2; M_1, M_2$ ) modes (and minor contribution from  $M_3$ -not shown), are shown in the inset of the same figure: here the vibrations are mostly due to Mo atom except for  $M_2$  where both Mo and Pt move (the complete list of the q-point and mode resolved phonon line widths are reported in the Supplementary Information).

Since Eq. (5) is commonly assumed to be valid in the range ( $\lambda \leq 2$  and  $\mu^* \leq 0.15$ ), it is clear that for such a large mass enhancement parameter it yields the wrong  $T_c$  that is actually two times larger than the experimental value  $T_c^{\text{exp}} = 4.7, 4.5 \text{ K}$  [30,32] with  $\mu^* = 0.15$ . The experimental transition temperature,  $T_c = 4.54 \text{ K}$ , can be recovered only by employing an exceptionally large Coulomb pseudopotential value  $\mu^* = 0.39$  (out of the validity range of the Allen-Dynes equation). We remind, however that in the original formulation of the Allen-Dynes formula extended to large  $\lambda$  values the same authors included two corrective factors, namely a “strong-coupling correction”  $f_1$  and a “shape correction”  $f_2$ . In particular considering just the “strong coupling” correction

$$f_1 = \left(1 + \frac{\lambda}{2.46(1 + 3.8\mu^*)}\right)^{3/2} \quad (8)$$

(the Eliashberg spectral function is calculated from ab-initio and thus is assumed to have the correct shape) we obtain  $T_c = 4.59\text{K}$  with  $\mu^* = 0.15$ , in nice agreement with the experiment. It is clear that the need of a strong coupling correction (or the usage of exceptionally large  $\mu^*$  values) is symptomatic that d-electrons decoupling should occur, and this should be related to the direct electron-electron pairing through suitable models such as the Hubbard-Emery one [38]. This model has been successfully employed to recover the Matthias rule in A-15  $A_3B$  superconductors (A transition metal, B non transition metal) [32] and, due to the stronger d-electron localization, it is likely that direct d-electron coupling or de-coupling play an even more important role in transition metals  $A_3B$  compounds. Anharmonicity as a possible cause of the large Coulomb pseudopotential in  $\text{Mo}_3\text{Pt}$  only is unlikely because there are no reasons why  $\text{Mo}_3\text{Os}$  should not be affected as well.

The total and q-point resolved spectral functions for  $\text{Mo}_3\text{Ir}$  are shown in Fig. 9(b). Contrarily to the previous two cases, there are no leading modes with enhanced coupling at the X and M (see the Supplementary Information for a complete list). Moreover, there is some coupling at (or close to) the  $\Gamma$ -point (see Table 4 and the inset of Fig. 9(b)) through  $T_{1g}$  modes (with just Mo atoms moving), and, at lesser extent,  $A_{2g}$  and  $E_g$  modes. All these modes, however, vibrate at relatively large frequencies, thus giving little contributions to the whole value of the mass enhancement parameter that, indeed is rather small with  $\lambda = 0.52$  (see Table 4). Thus, in spite of the large  $\omega_{\text{log}}$  value, the predicted transition temperature is wrong ( $T_c = 1.6\text{K}$  with  $\mu^* = 0.15$ ) as compared to the experiments  $T_c^{\text{exp}} = 9.1, 8.5\text{K}$  [30,32]. The experimental transition temperature can be recovered only by employing an exceptionally low Coulomb pseudopotential  $\mu^* = 0.01$  thus obtaining  $T_c = 9.06\text{K}$ . In this case therefore, strong local correlations of d-electrons should play a leading role either for direct coupling or by cooperating with phonon-mediated pairing. The present model, however, does not include phenomena, such as the direct coupling or vertex corrections due to the electron interactions with collective excitations, that might account for strong correlation or correlation enhanced phonon mediated pairing [39]. It appears, hence, that  $\text{Mo}_3\text{Ir}$  superconductivity is mostly related to correlations of d-electrons rather than on phonon mediated pairing.

### 3.3. Under compression

Exploring the properties of the materials under compression (pressure) is always an interesting phenomena for all the researchers. Previously, some experimental and theoretical studies have reported ETT in some of the Nb based compounds by highlighting the anomalies evidenced in the Fermi surface topology, together with non-monotonic variation in the total density of states at the  $E_F$  under compression [40]. It is expected that the variation in superconducting transition temperature would be non-monotonic, if there exists an ETT under pressure as seen earlier in several compounds [41], which may be possible in the compounds of present study also. In the present investigated compounds also, we have observed few of the Fermi surfaces to change under pressure in all the compounds at different compressions. For this study, we have compressed all the systems from  $V/V_0$  (relative volume) = 1.00 to 0.90 with an interval of 0.2. It is already well known that under compression, the availability of electrons near the  $E_F$  vary and will lead to changes in the position of the  $E_F$  and affect the electronic structure and physical properties of the system.

Fig. 2(a,d) shows the band structure of  $\text{V}_3\text{Os}$  at relative volume being 1.00 and 0.90 respectively and the corresponding Fermi surface topologies are shown in Fig. 3(a). A slight change in one of the Fermi surfaces is noticed as the radius of the hole pocket decreases for the relative volume corresponding to 0.90 at X-point as seen from band index 3 from Fig. 3(a). This change indicates the possibility of Electronic Topological Transitions (ETTs) in the studied compound at this compression (The possibility of an ETT is indicated by a dashed line from ambient to compressed volume in Fig. 3(a)). Fig. 2(b,e) shows the band structure of  $\text{V}_3\text{Ir}$  for the relative volume around 1.00 and 0.90 respectively and the corresponding Fermi surface topologies are shown in Fig. 3(b). The evolution of new Fermi surface in X-M direction at the relative volume around 0.90 as shown in the last Fermi surface in Fig. 3(b) indicates the ETT at this compression in this compound. Fig. 2(c,f) shows the band structure of  $\text{V}_3\text{Pt}$  at the relative volume around 1.00 and 0.90 respectively and the corresponding Fermi surface topologies are shown in Fig. 3(c). One can clearly observe a change in the Fermi surface when the relative volume is around 0.90 (because of the shifting of the third band from valence to conduction band shown in Fig. 2(f)) as shown in last Fermi surface of Fig. 3(c), which again confirms the presence of ETT under compression in this compound.

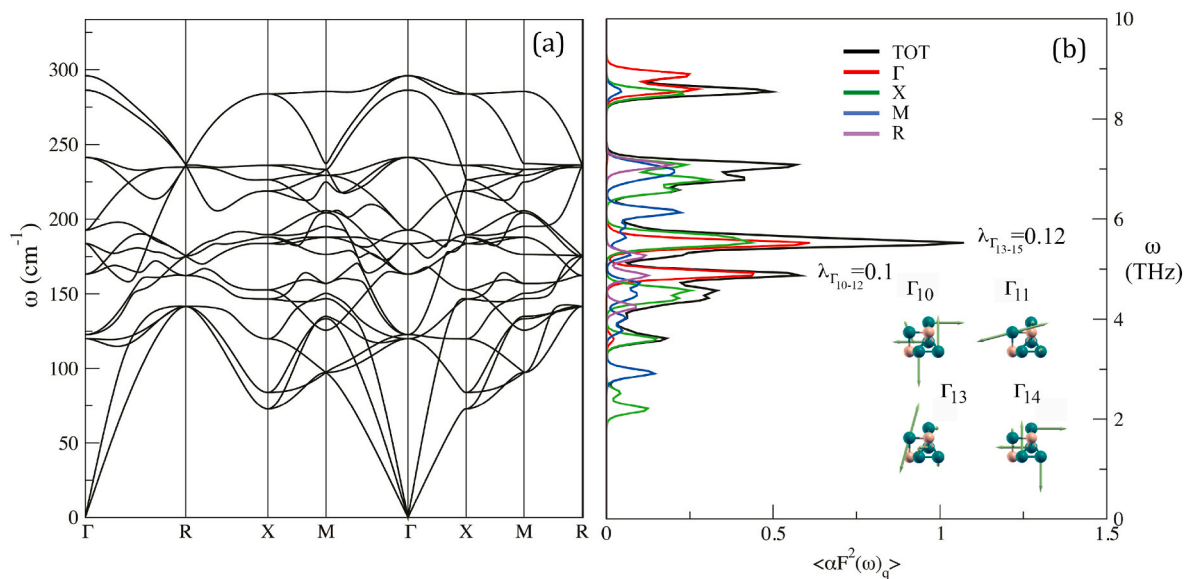


Fig. 9. Phonon dispersion (a) and total and q-point resolved spectral function (b) for  $\text{Mo}_3\text{Ir}$ . The most important vibrational eigen-vectors contributing to the phonon mediated coupling are drawn in the inset of (b). The peaks of the q-point resolved spectral function are labeled with the main mode and q-point resolved mass enhancement parameters  $\lambda_{q,v}$ .

Fig. 4(a,d) shows the band structure of Cr<sub>3</sub>O<sub>s</sub> corresponding to the relative volumes around 1.0 and 0.90 respectively and the corresponding Fermi surface topologies are shown in Fig. 6(a). The size of the Fermi surface pocket at X decreases when the relative volume approaches 0.90, which can be seen in last Fermi surface from Fig. 6(a) due to the upward shift in third band at X-point as shown in Fig. 4(d). Fig. 4(b,e) shows the band structure of Cr<sub>3</sub>Ir corresponding to the relative volumes 1.0 and 0.90 respectively and the corresponding Fermi surface topologies are shown in Fig. 6(b). The third band as shown from Fig. 4(e) undergoes changes at X-M and  $\Gamma$ -X directions leading to noticeable change in the corresponding Fermi surface at  $V/V_0 = 0.90$  as shown in last Fermi surface from Fig. 6(b) leading to an ETT. Fig. 4(c,f) shows the band structure of Cr<sub>3</sub>Pt at relative volumes corresponding to 1.0 and 0.90 respectively and the corresponding Fermi surface topologies are shown in Fig. 6(c). As there is a significant downward shift in the fourth band along M-R direction seen from Fig. 4(f), one can clearly observe the evolution of Fermi surface around X-M-R at compressed volume around 0.90 as shown in last Fermi surface from Fig. 6(c). All the above observed changes in the Fermi surface for Cr<sub>3</sub>Y again confirm the presence of ETT under compression in these compounds.

In case of Mo based compounds, we have also observed a similar nature at different compressions. Fig. 5(a,d) shows the band structure of Mo<sub>3</sub>O<sub>s</sub> corresponding to the relative volumes around 1.0 and 0.92 respectively. For Mo<sub>3</sub>O<sub>s</sub> compound, the maximum change is observed only in second Fermi surface at the relative volume around 0.92 as seen in last Fermi surface from Fig. 6(d), where we observed the presence of sheet along M-X direction compared to ambient due to the upward shift of second band along M-X direction which is shown in Fig. 5(d). Fig. 5(b, e) shows the band structure of Mo<sub>3</sub>Ir corresponding to the relative volumes 1.0 and 0.98 respectively. In Mo<sub>3</sub>Ir, we have observed an increase in the size of the pockets along R-F at relative volume corresponding to 0.98 as shown in last Fermi surface from Fig. 6(e) and the remaining Fermi surfaces are not affected much. Fig. 5(c,f) shows the band structure of Mo<sub>3</sub>Pt corresponding to the relative volumes 1.0 and 0.90 respectively. In Mo<sub>3</sub>Pt, we have observed the closing of the gap at X-point in the fifth Fermi surface, when the relative volume reaches 0.94 and also for subsequent compressions as shown in Fig. 6(f). In addition, we also observed the absence of final Fermi surface, at relative volume being 0.90, which was present at ambient. All these above changes account for the observed ETTs in the present compounds at different compressions.

We have studied the effect of pressure on the density of states, at  $E_F$  and are shown in Fig. S7 for the compounds under study. From Fig. S7, it is evident that there is a non-monotonic variation observed in DOS of V<sub>3</sub>O<sub>s</sub> and V<sub>3</sub>Pt, while there is an increase in DOS observed for V<sub>3</sub>Ir compound under pressure. For Cr<sub>3</sub>O<sub>s</sub>, Cr<sub>3</sub>Ir and Cr<sub>3</sub>Pt compounds, non-monotonic variation of DOS is observed under compression. In similar manner, in the case of Mo<sub>3</sub>O<sub>s</sub> and Mo<sub>3</sub>Pt, the total DOS at  $E_F$  decreases with volume compression and opposite nature is observed in Mo<sub>3</sub>Ir under compression as shown in Fig. S7. This gives a hint that non-monotonic variation in DOS may lead to non-monotonic variation in  $T_c$  as stated in earlier literature [40] and needs to be verified.

To check the mechanical stability under compression, single crystalline elastic constants are computed and details are given in Fig. S8 for the compounds under study. From the plots, it is seen that calculated values follow an increasing trend under pressure and the effect is found to be more marked in  $C_{11}$  and less evident in  $C_{44}$  in all the investigated compounds. We have also analyzed the same effect on the shear modulus  $C_s$  for all the compounds under compression and plotted it along with the single crystalline elastic constants to check the possibility of ETTs in all the investigated compounds. A non-linear nature is observed in  $C_{44}$  and  $C_s$  elastic constants under pressure, which confirms the presence of ETTs in the present compounds. From the present and previous observations, it may be confirmed that the ETT may be common in all the A-15 compounds under compression.

## 4. Conclusions

Ab-initio calculations are performed for X<sub>3</sub>Y (X = V, Cr, Mo; Y = Os, Ir and Pt) compounds both at ambient and high pressure. The 'd' states of both the atoms contribute to a greater extent at the  $E_F$ . Mechanical stability is confirmed from the computed single crystal elastic constants both at ambient and under compression. The phonon dispersion spectra confirm the dynamical stability of the compounds. ETTs are observed in all these studied compounds under pressure. This may be a common feature in these A-15 type of compounds under the effect of pressure. The phonon-mediated formation of Cooper pairs has been studied through DFT-based Eliashberg theory of the electron-phonon coupling for the Mo<sub>3</sub>Y (Y = Os, Ir and Pt) series, that is the one with the largest superconducting transition temperature. The mass enhancement parameter  $\lambda$ , that is the key quantity describing the phonon-mediated superconductivity, returns, through the Mc Millan formula the transition temperature. Among the three compounds studied, only Mo<sub>3</sub>O<sub>s</sub> is fully consistent with the adopted theoretical scheme evidencing that superconductivity in this compound is definitely phonon-mediated. Mo<sub>3</sub>Pt can be also interpreted in the Eliashberg theory provided a correction for strong coupling is applied while Mo<sub>3</sub>Ir appear markedly affected by strong correlation effects of d-electrons and thus require more sophisticated approaches such as vertex corrections, strong coupling to local spin configurations or full first-principles methods (SCDFT).

## Author contributions

P. Rambabu: Software, Methodology, Validation, Visualization, writing, review and editing.

Giuseppe Zollo: Conceptualization, Software, Methodology, Validation, Visualization, writing, review and editing.

V. Kanchana: Conceptualization, Software, Methodology, Validation, Visualization, Project administration, writing, review and editing.

## Declaration of competing interest

The authors declare that they have no known competing financial interests or personal relationships that could have appeared to influence the work reported in this paper.

## Acknowledgement

The authors PR and VK would like to thank IIT Hyderabad and National PARAM Supercomputing Facility (NPSF) and Center for Development of Advanced Computing (C-DAC), Pune for computational facility and PR acknowledges Guru Ghasidas Vishwavidyalaya, Bilaspur, C.G. for sponsoring Ph.D. PR would also like to acknowledge Peram V. Sreenivasa Reddy for the initial set of calculations. The author GZ would like to acknowledge CRESCO/ENEAGRID High Performance Computing infrastructure and its staff [42] for providing some computational resources. CRESCO/ENEAGRID HPC infrastructure is funded by ENEA, the Italian National Agency for New Technologies, Energy and Sustainable Economic Development and by Italian and European research programmes, see <http://www.cresco.enea.it/english> for information.

## Appendix A. Supplementary data

Supplementary data to this article can be found online at <https://doi.org/10.1016/j.jpcs.2021.109953>.

## References

- [1] (a) E.Z. Kurmaev, F. Werfel, O. Brümmer, R. Flükiger, *Solid State Commun.* 21 (1977) 239–243; (b) E.Z. Kurmaev, et al., *Phys. Status Solidi* 61 (1974) 365 (b); (c) E.Z. Kurmaev, V.P. Belash, R. Flükiger, A. Junod, *Solid State Commun.* 16

- (1975) 1139;  
 (d) R.A. Pollak, C.C. Tsuei, R.W. Johnson, *Solid State Commun.* 23 (1977) 879–881;  
 (e) A. Junod, T. Jarlborg, T. Muller, *Phys. Rev. B* 27 (1983) 1568.
- [2] B.M. Klein, L.L. Boyer, D.A. Papaconstantopoulos, L.F. Mattheiss, *Phys. Rev. B* 18 (1978) 6411–6438.
- [3] C. Paduani, *Physica B* 393 (2007) 105–109.
- [4] G. Subhashree, S. Sankar, R. Krithiga, *Mod. Phys. Lett. B* 28 (2014) 1450233.
- [5] R.A. Hein, J.E. Cox, R.D. Blaugher, R.M. Waterstrat, *Solid State Commun.* 7 (1969) 381–384.
- [6] H.M. Tutuncu, H.Y. Uzunok, G.P. Srivastava, V. Ozdemir, G. Ugur, *Intermetallics* 96 (2018) 25–32.
- [7] F. Gala, G. De Marzi, L. Muzzi, G. Zollo, *Phys. Chem. Chem. Phys.* 18 (2016) 32840.
- [8] A.P. Cracknell, K.C. Wang, *The Fermi Surface: its Concept, Determination and Use in the Physics of Metals*, Oxford University Press, 1973.
- [9] L. Van Hove, *Phys. Rev. B* 89 (1953) 1189–1193.
- [10] H. Ghosh, S. Sen, *J. Alloys Compd.* 677 (2016) 245–251.
- [11] T. Jarlborg, A. Bianconi, *Sci. Rep.* 6 (2016) 24816.
- [12] Y. Zhang, C. Wang, Li Yu, G. Liu, A. Liang, J. Huang, S. Nie, X. Sun, Yuxiao Zhang, B. Shen, J. Liu, H. Weng, L. Zhao, G. Chen, X. Jia, C. Hu, Y. Ding, W. Zhao, Q. Gao, C. Li, S. He, L. Zhao, F. Zhang, S. Zhang, F. Yang, Z. Wang, Q. Peng, X. Dai, Z. Fang, Z. Xu, C. Chen, X.J. Zhou, *Nat. Commun.* 8 (2017) 15512.
- [13] Z.J. Xiang, G.J. Ye, C. Shang, B. Lei, N.Z. Wang, K.S. Yang, D.Y. Liu, F.B. Meng, X. G. Luo, L.J. Zou, Z. Sun, Y. Zhang, X.H. Chen, *Phys. Rev. Lett.* 115 (2015) 186403.
- [14] Su-Yang Xu, C. Liu, I. Belopolski, S.K. Kushwaha, R. Sankar, J.W. Krizan, T. R. Chang, C.M. Polley, J. Adell, T. Balasubramanian, K. Miyamoto, N. Alidoust, G. Bian, M. Neupane, H.T. Jeng, C.Y. Huang, W.F. Tsai, T. Okuda, A. Bansil, F. C. Chou, R.J. Cava, H. Lin, M.Z. Hasan, *Phys. Rev. B* 92 (2015), 075115.
- [15] Fei-Xiang Xiang, Xiao-Lin Wang, Menno Veldhorst, Shi-Xue Dou, Michael S. Fuhrer, *Phys. Rev. B* 92 (2015), 035123.
- [16] I. Efthimiopoulos, C. Buchan, Y. Wang, *Sci. Rep.* 6 (2016) 24246.
- [17] P.V. Sreenivasa Reddy, V. Kanchana, G. Vaitheeswaran, P. Modak, A.K. Verma, *J. Appl. Phys.* 119 (2016), 075901.
- [18] J.P. Perdew, K. Burke, M. Ernzerhof, *Phys. Rev. Lett.* 77 (1996) 3865.
- [19] P. Blaha, K. Schwarz, P. Sorantin, S.B. Tricky, *Comput. Phys. Commun.* 59 (1990) 399.
- [20] H.J. Monkhorst, J.D. Pack, *Phys. Rev. B* 13 (1976) 5188.
- [21] P. Blöchl, O. Jepsen, O. Andersen, *Phys. Rev. B* 49 (1994) 16223.
- [22] F. Birch, *Phys. Rev.* 71 (1947) 809.
- [23] A. Togo, I. Tanaka, *Scripta Mater.* 108 (2015) 1–5.
- [24] G. Kresse, D. Joubert, *Phys. Rev. B* 59 (1999) 1758–1775.
- [25] M. Wierzbowska and S. de Gironcoli and P. Giannozzi, arXiv:cond-mat/05024077 (2006).
- [26] P. Giannozzi, et al., *J. Phys. Condens. Matter* 21 (2009) 395502.
- [27] M. Born, *J. Chem. Phys.* 7 (1939) 591.
- [28] M.I. Naher, F. Parvin, K.M. Azharul, A. Islam, SalehH. Naqib, *Eur. Phys. J. B* 91 (2018) 289.
- [29] M. Enamul Haque, Anwar Hossain, *J. Alloys Compd.* 739 (2018) 737–745.
- [30] P. Charles, Poole Jr. (Eds.), *Handbook of Superconductivity*, Academic Press, 2000.
- [31] B.T. Matthias, T.H. Geballe, V.B. Compton, *Rev. Mod. Phys.* 35 (1963) 1.
- [32] R.O. Zaitsev, Yu V. Mikhailova, *J. Exp. Theor. Phys.* 91 (3) (2000) 568–578.
- [33] C. Hartwigsen, S. Goedecker, J. Hutter, *Phys. Rev. B* 58 (1998) 3641.
- [34] W.L. McMillan, *Phys. Rev.* 167 (1968) 331.
- [35] P.B. Allen, R.C. Dynes, *Phys. Rev. B* 12 (1975) 905.
- [36] K.H. Bennemann, J.W. Garland, H.C. Wolfe, D.H. Douglass, *AIP Conf. Proc* 4 (1972) 103–137.
- [37] A.P. Koufos, D.A. Papaconstantopoulos, M.J. Mehl, *Phys. Rev. B* 89 (2014) 35150.
- [38] V.J. Emery, *Phys. Rev. Lett.* 58 (1987) 2794.
- [39] M. Mierzejewski, J. Zielinski, *J. Supercond.* 11 (1998) 331.
- [40] P.V. Sreenivasa Reddy, V. Kanchana, *J. Phys. Condens. Matter* 29 (2017) 405502.
- [41] S. Ram, V. Kanchana, G. Vaitheeswaran, A. Svane, S.B. Dugdale, S.E. Christensen, *Phys. Rev. B* 85 (2012) 174531.
- [42] F.Iannone, F.Ambrosino, G.Bracco, M.DeRosa, A. Funel, G. Guarnieri, S. Migliori, F. Palombi, G. Ponti, G. Santomauro et al. in booktitle2019 International Conference on High Performance Computing Simulation (HPCS) (year2019), pp. pages1051–1052.